MICROSTRUCTURES IN FRICTION STIR WELDED 304 AUSTENITIC STAINLESS STEEL

H. Kokawa[1], S.H.C. Park[1], Y.S. Sato[1],
K. Okamoto[2], S. Hirano[2], M. Inagaki[2]
[1]Department of Materials Processing, Graduate School of Engineering, Tohoku University
[2]Hitachi Research Laboratory, Hitachi Ltd.
(Japan)

ABSTRACT

Friction stir welding was applied to 304 austenitic stainless steel. The microstructural evolution and hardness distribution in the weld were investigated. The stir zone (SZ) and thermomechanically affected zone (TMAZ) showed dynamically recrystallised and recovered microstructures, respectively. The hardness of the SZ was higher than that of the base material and the maximum hardness was located in the TMAZ. The higher hardness in TMAZ was attributed to high density of dislocations and sub-grains. Electron microscopic observations revealed that ferrite and sigma phase were formed in austenite matrix in the SZ depending on the cooling rate during FSW.

IIW-Thesaurus keywords: *Friction stir welding; Friction welding; Stainless steels; Steels; Microstructure; Grain size; Hardness; Mechanical properties; Austenite; Ferrite; Recrystallisation; Reference lists.*

1 INTRODUCTION

A wide range of investigations have been carried out on Friction Stir Welding (FSW), which is an innovative joining process utilizing frictional heating and intensive plastic deformation [1,2]. Researchers have been studying microstructures [3,4], mechanical properties [5,6], corrosion properties [7] of friction stir (FS) welds, and plastic flows [8,9] during FSW. FSW provides good mechanical properties in high strength aluminium (Al) alloys and exhibits good weldability in joining dissimilar materials [10-12]. Furthermore, FSW often draws attention as an effective method for improving the mechanical properties in the stir zone (SZ) because the SZ experiences dynamic recrystallisation during FSW and often shows fine recrystallised grain structure [13-15]. However, most published papers on FSW have been focussed on relatively low melting temperature materials such as Al alloys and magnesium alloys.

Recently, the feasibility of FSW for stainless and mild steels with higher melting temperatures has been examined and reported, and further revitalization of research and development is advancing FSW [16-20]. Our research group has investigated on the feasibility of FSW in stainless steels and reported that FSW offers a sound weld joint in austenitic, ferritic and duplex stainless steels [21]. Austenitic stainless steels are widely used in nuclear power plant circumstances requiring high temperature components such as heat exchanger and chemical reactors because of their good mechanical properties at elevated temperatures and excellent corrosion resistance. Austenitic stainless steel welds, however, have problems in stress corrosion cracking and weld decay due to sensitisation in heat-affected zone. FSW has the potential to offer weld with a minimal heat-affected zone, small residual stress and distortion, no crack and macro-segregation due to solidification, and a finely recrystallised microstructure. For these reasons, we have been conducting FSW of austenitic stainless steels and reported the characteristics of microstructures in FS welds of type 304 austenitic stainless steel. This paper discussed the microstructural evolution during FSW in FS weld of 304 austenitic stainless steel by reviewing our recent studies [19,22].

2 EXPERIMENTAL PROCEDURE

Two different thick 304 austenitic stainless steel plates with 2 mm and 6 mm in thickness were used as base material (BM) in this study. The nominal chemical compositions (wt %) of the plates are 17.93 Cr, 8.28 Ni, 0.47 Si, 0.78 Mn, 0.072 C, 0.030 P, 0.005 S for the 2 mm-thick plate and 18.10 Cr, 8.56 Ni, 0.59 Si, 1.08 Mn, 0.040 C, 0.032 P, 0.003 S for the 6 mm-thick plate. FSW was carried out for each of the two BM plates using a polycrystalline cubic boron nitride (PCBN) tool [23] tilted 3.5 degrees from vertical. The FSW parameters of travelling-rotation speeds of tool were 4.5 mm/s – 1 300 rpm for the 2 mm-thick plate and 1.3 mm/s – 550 rpm for the

Doc. IIW-1671-04 (ex-doc. III-1300-04/IX-2093-04) recommended for publication by Commission III “Resistance welding, solid state welding and allied joining processes” and Commission IX “Behaviour of metals subjected to welding”.

6 mm-thick plate. Vickers hardness profile of the weld was measured on the cross section perpendicular to the welding direction (WD). Microstructural observations were performed by optical microscopy (OM), transmission electron microscopy (TEM) and orientation imaging microscopy (OIM). The specimens for OM were cut perpendicular to the WD, mechanically ground with water abrasive paper and polished with 3 μm and 1 μm diamond, and etched electrolytically in a solution of 10 % oxalic acid + 90 % water with a power supply set to 30 volts for about 10 s. Thin disks for TEM with a diameter of 3 mm were cut from various locations of the welds using an electrical-discharge machine, and were electrolytically polished in a 10 % perchloric acid + 90 % ethanol solution. The thin foils were observed at 200 kV with a JEOL-2000EXII TEM. Identification of the second phases in the austenite matrix was determined from selected area electron diffraction patterns. In order to measure the grain size in various locations of the weld and distinguish between ferrite and austenite in large-scaled areas of the SZ, OIM analysis was carried out. The sample for OIM was prepared by electrolytical polishing with the same solution used for the preparation of the TEM sample. The grain size in the various regions was measured in OIM maps by the mean linear intercept method.

3 RESULTS AND DISCUSSION

3.1 Microstructures in FS weld

Figure 1 shows a low magnification overview of the cross section in a FS weld of 2 mm-thick 304 stainless steel. Since the length of the pin of the welding tool was shorter than the thickness of the plate, the pin could not fully penetrate the plate. The width of the SZ in upper surface of the plate is about 10 mm, which roughly corresponds to the diameter of the shoulder. The SZ does not take the form of an elliptical nugget with an onion ring pattern. Small tunnel-type defects are seen around the border between the SZ and the TMAZ at the advancing side (AS) as shown in Figure 2 where a darkly etched region is observed near the tunnel-type defects indicated by arrows. The dark region is discussed later.

The optical micrographs and TEM images of several regions in the 2 mm-thick FS weld are shown in Figures 3 (a)-(d) and 4 (a)-(d), respectively. The regions observed by OM and TEM are indicated in Figure 1. The BM has an annealed grain structure with a low density of dislocations. Annealing twin boundaries are also observed in some grains. The average grain size of the BM was about 8.8 μm. The SZ shows a roughly equiaxed grain structure. Dislocation density in the SZ is slightly higher than that in the BM. The average grain size in the SZ was 7.0 μm, which is slightly smaller than that in the BM. It is also detected in the SZ that small grains with a very low density of dislocations coexist with grains containing dislocations. This means that dynamic recrystallisation occurred in the SZ induced by the intense plastic deformation and accompanying frictional heating during FSW. On the other hand, the TMAZs in both the retreating and the advancing sides (RS and AS) have a grain structure with a relatively high density of sub-boundaries and dislocations, as shown in Figures 4 (b) and (d). These micrographs suggest that the TMAZs are characterised by dynamic recovery, which is in good agreement with the typical microstructural characteristics in FS welds of Al alloys [4].

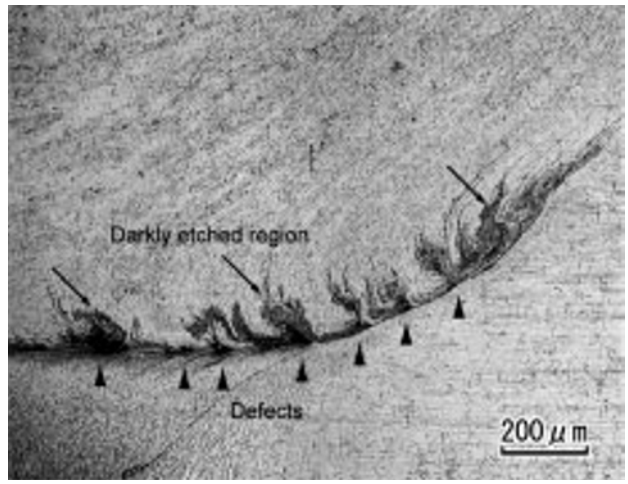

Figure 2 – Defects in the advancing side of the stir zone in Figure 1

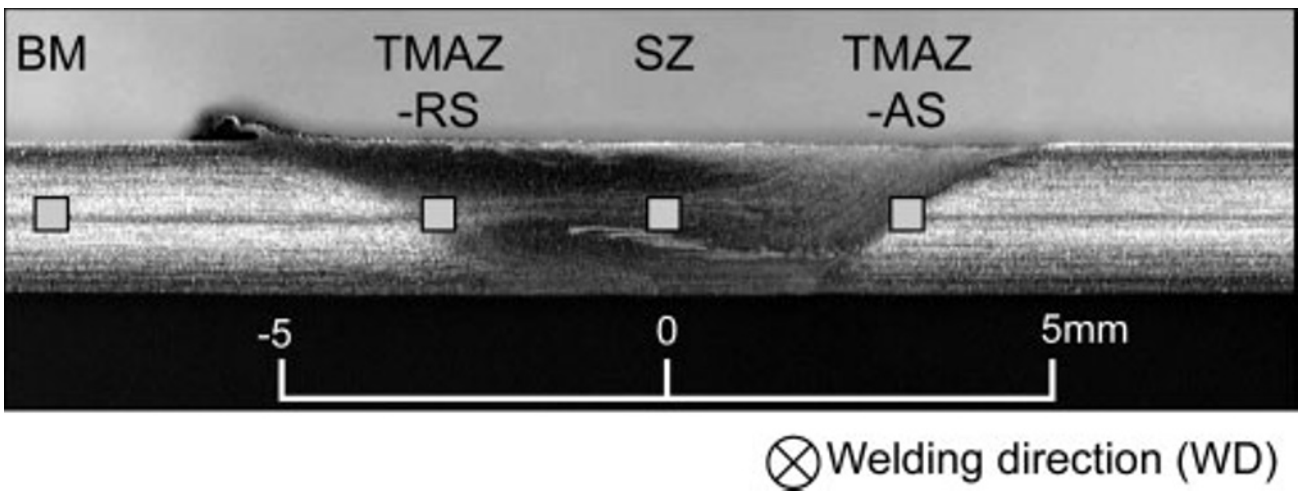

Figure 1 – Macroscopic cross sectional view of the 2 mm-thick FS weld

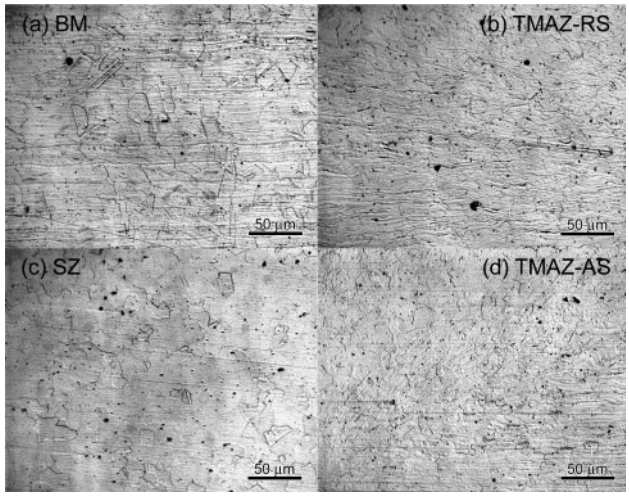

Figure 3 – Optical microstructures in (a) BM, (b) TMAZ of retreating side (RS), (c) SZ, (d) TMAZ of advancing side (AS) in 2 mm-thick weld

The hardness distribution across the transverse direction in the 2 mm-thick weld is shown in Figure 5. The average hardness value of the BM is 180 Hv. The weld shows higher hardness than the BM. The hardness of the weld increases from the unaffected BM region toward the TMAZ. The maximum hardness is measured in the TMAZ about 3 mm apart from the weld centre. The hardness of the SZ is slightly lower than that of the TMAZ.

The grain size distribution measured by mean intercept method for the OIM maps is shown in Figure 6. The SZ has smaller average grain size than the BM although the grain size is slightly scattered in the weld. The TMAZ has slightly finer grain size than the BM. It is well known that finer grain size generally results in higher hardness. According to the Hall-Petch relationship for hardness in 304 stainless steel [24], the difference in hardness between the BM and the SZ should be 10 Hv and the difference between the BM and the TMAZ should be 5 Hv. However, the weld has a hardness difference of about 20 Hv between the BM and the SZ and a difference of about 30 Hv between the BM and the TMAZ, which does not agree with estimates from the Hall-Petch relationship. This means that the increase in hardness

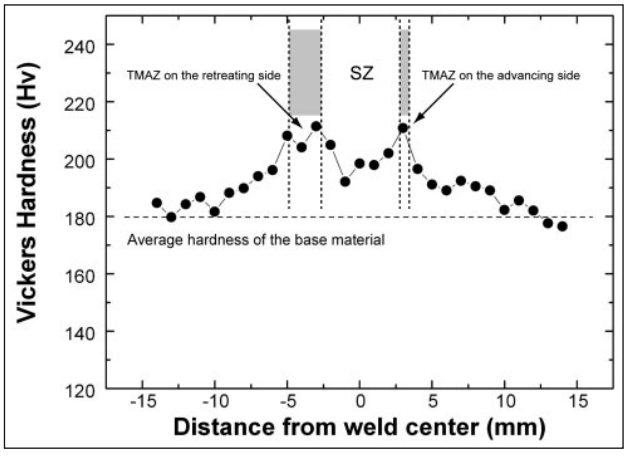

Figure 5 – Hardness profile in the 2 mm-thick weld

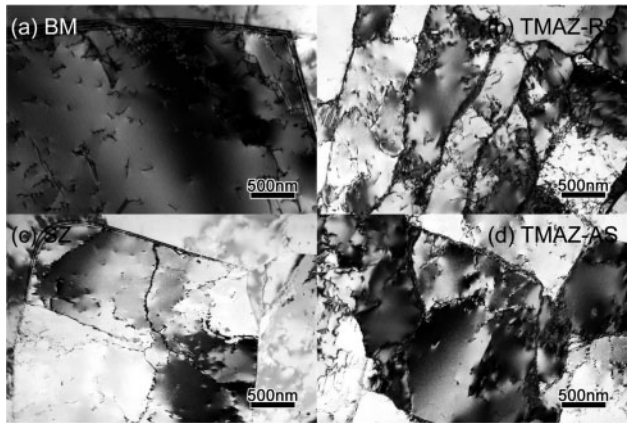

Figure 4 – TEM images of corresponding regions in Figure 3

in the weld cannot be explained by grain size alone. Besides the grain size distributions, in the present weld, dislocation density may also affect the hardness distribution, because dislocation densities in the SZ and the TMAZ are higher than that in the BM, as shown in Figure 4. Additionally, the TMAZ has many sub-grains, which also cause an increase in hardness. These results suggest that the high dislocation density and sub-grains formed during dynamic recrystallisation and recovery processes result in a higher hardness in the SZ and the TMAZ.

3.2 Ferrite and sigma formation during FSW

A darkly etched microstructure was observed around the defects in the 2 mm-thick weld, as shown in Figure 2. The details of the darkly etched microstructures observed in three different locations of the SZ are shown in Figure 7. Besides the region around the defects [Figure 7 (a)], the region near the weld centre [Figure 7 (b)] also has a darkly etched microstructure. High magnification observation reveals that the darkly etched microstructure is finely scattered in the advanc-

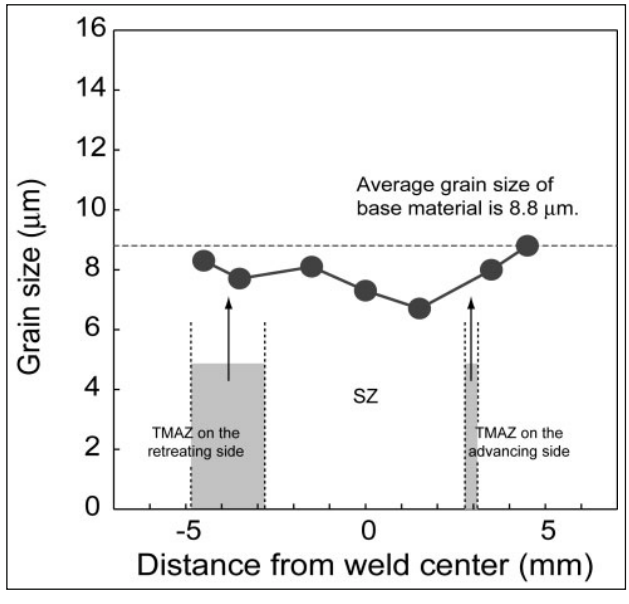

Figure 6 – Grain size distribution in the 2 mm-thick weld by OIM

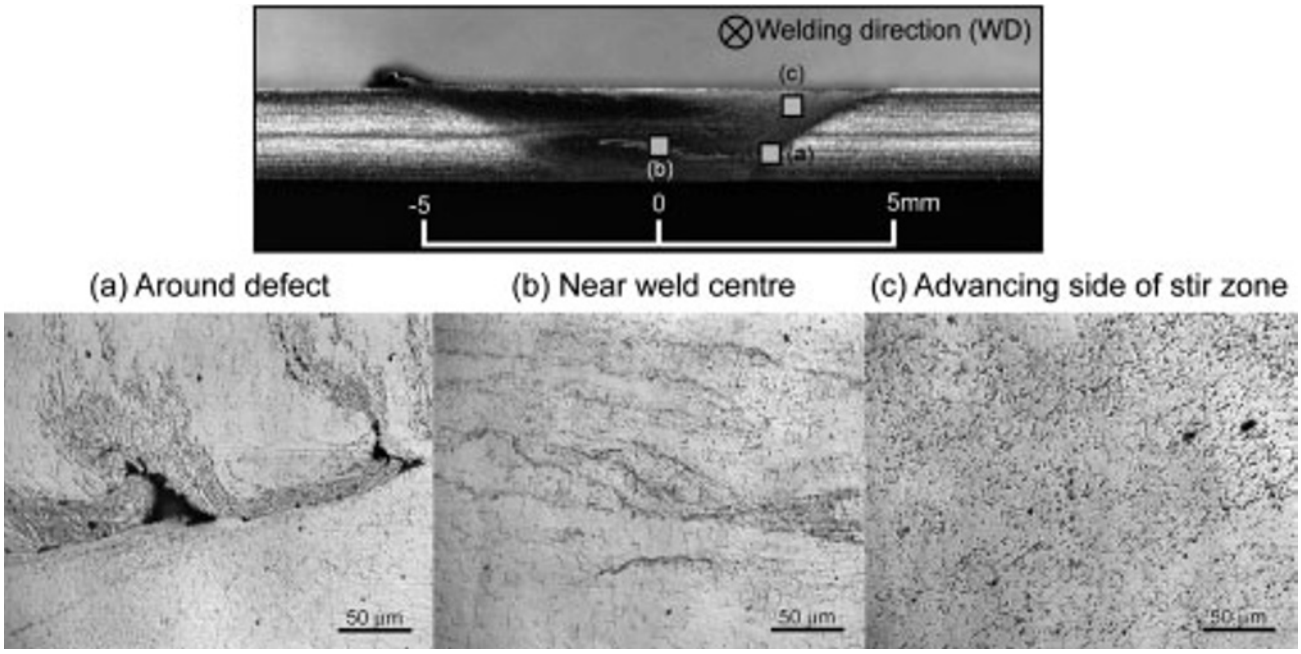

Figure 7 – Optical micrographs of darkly etched regions (a) around the defect, (b) near the weld centre, (c) the advancing side of the stir zone in the 2 mm-thick weld

ing side of the SZ, as shown in Figure 7 (c). The darkly etched microstructure seems to be widely and inhomogeneously distributed in the SZ. In order to identify the darkly etched microstructure, OIM analysis was carried out on the above-mentioned three regions. During OIM data collection, austenite (fcc) and ferrite (bcc) data files were used as references, because there is a high possibility that the austenite matrix is transformed to delta-ferrite by the exposure to high temperatures during the welding process. The OIM maps obtained from the above-mentioned three regions are indicated in Figure 8. Austenite (fcc) and ferrite (bcc) are indicated with gray and white in the OIM maps, respectively. Figure 8 shows that small ferrite phases, about 1 μm in size, are formed along the grain boundaries and at their triple junctions in the austenite matrix in these regions. The size of the ferrite phase is slightly larger near the weld centre, as shown in Figure 8 (b).

The detection and identification of ferrite was also performed in the advancing side of the SZ by selected area electron diffraction pattern in the TEM. Figure 9 presents that the ferrite phases are formed along the grain boundaries of the recrystallised austenite matrix in the advancing side of the SZ. Most of the ferrite has an elongated shape, whose dimension is smaller than 1 μm in width and about 2 μm in length. This result is roughly the same as that of the OIM analysis. The ferrite phases observed in the present weld are thought to be formed by heating to high temperatures during FSW.

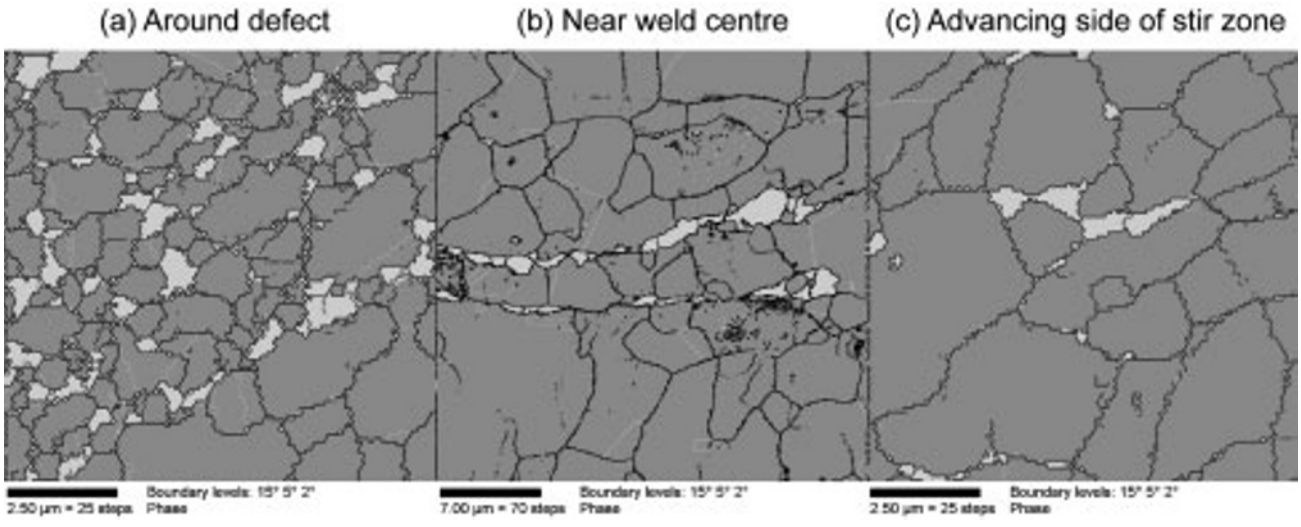

Grey and white colours indicate austenite matrix and ferrite formed along the grain boundary, respectively.

Figure 8 – OIM maps in darkly etched regions (a) around the defect, (b) near the weld centre, (c) the advancing side of the stir zone in the 2 mm-thick weld

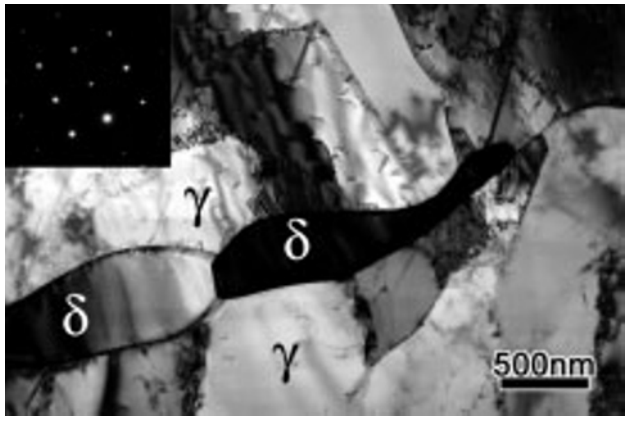

Figure 9 – TEM images of ferrite formed along the grain boundary of the austenite matrix in the advancing side of the stir zone

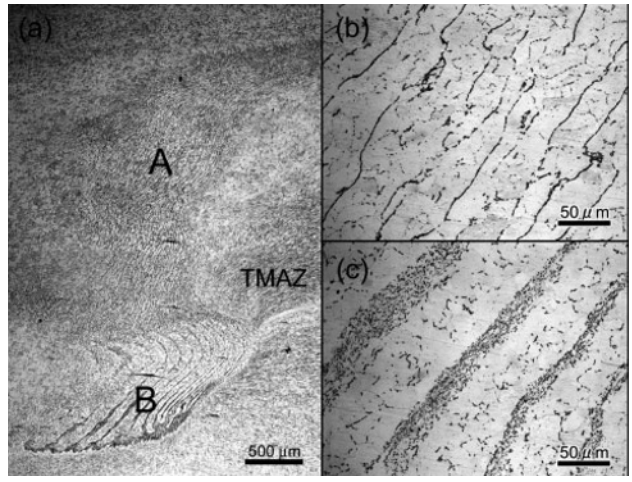

Figure 10
(a) Cross sectional view of the stir zone at the advancing side in the 6 mm-thick weld
(b) Detailed microstructure of region "A"
(c) Detailed microstructure of region "B"

The microstructural characteristics in the 6 mm-thick weld are qualitatively identical to those in the 2 mm-thick weld, except for sigma formation at the advancing side instead of ferrite, as described as follows. Band structures at the advancing side were observed in the 6 mm-thick weld as shown in Figure 10. The band structures can be divided into region "A" and region "B", as shown in Figure 10 (a). Detailed micrographs of regions "A" and "B" are shown in Figure 10 (b) and (c), respectively. Region "A" has deeply etched lines, while region "B" shows a lamellar structure consisting of a region with many pits and a region without pits. The lamellar structure in region "B" looks like a segment of an onion ring which is frequently observed in Al and Mg alloy FS welds [25].

The OIM maps and TEM images of regions "A" and "B" are shown in Figure 11. Figure 11 (b) reveals that large particles with size of 500-1 000 nm exist on the grain boundaries in region "A". On the other hand, the OIM map of region "B" showed that the regions with many pits in the lamellar structure correspond to regions consisting of finer grains, as shown by the arrows in Figure 11 (d). Additionally, a TEM image [Figure 11 (e)] indicates that the regions with many pits have small particles with size of 200-400 nm both along the grain boundaries and in the grain interiors. EDS spectra obtained from the particles in regions "A" and "B" are presented in Figure 11 (c) and (f), respectively. The large particles in region "A" consist of 54.6 wt % Cr, 43.1 wt % Fe and 1.0 wt % Ni, while the small particles in region "B" consist of 33.8 wt % Cr, 60.6 wt % Fe and 5.0 wt % Ni. EDS results suggest that these particles should be Cr-rich carbides or sigma phases. Higher

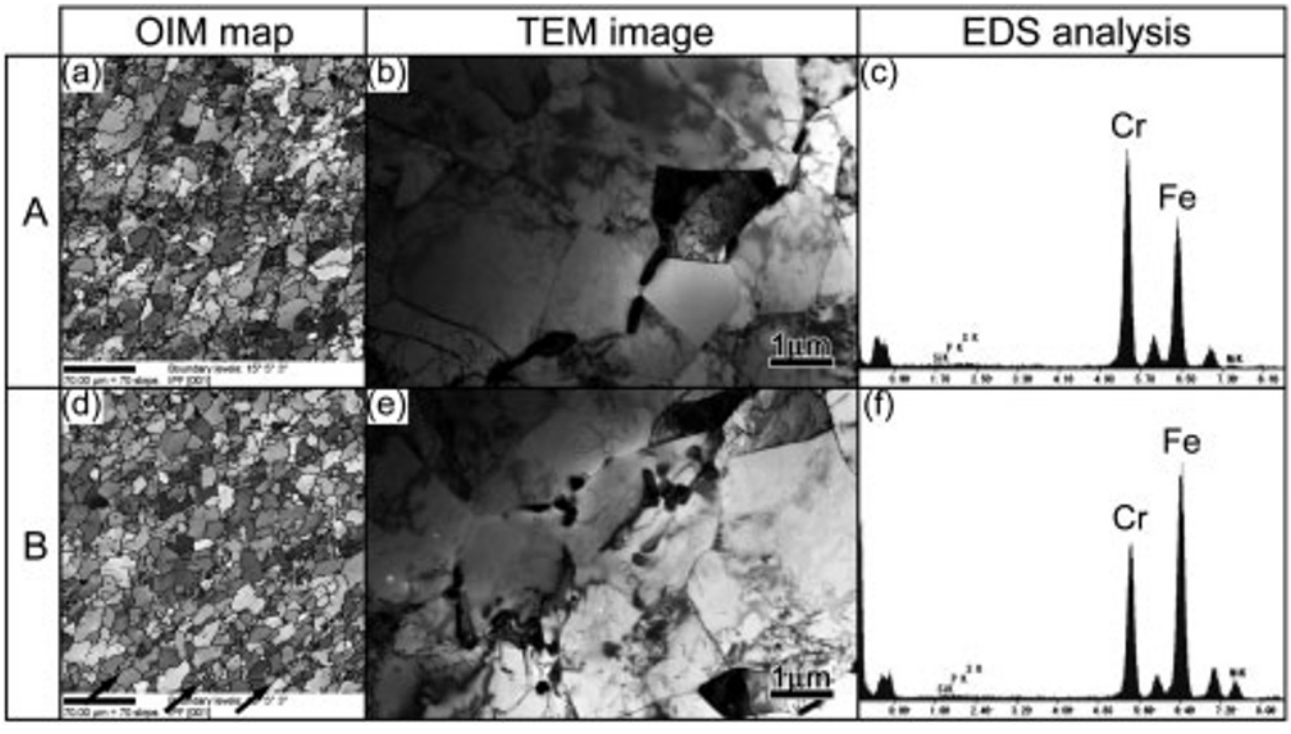

Figure 11 – Typical OIM maps and TEM images in regions "A" and "B" and EDS analyses in the regions of Figure 10

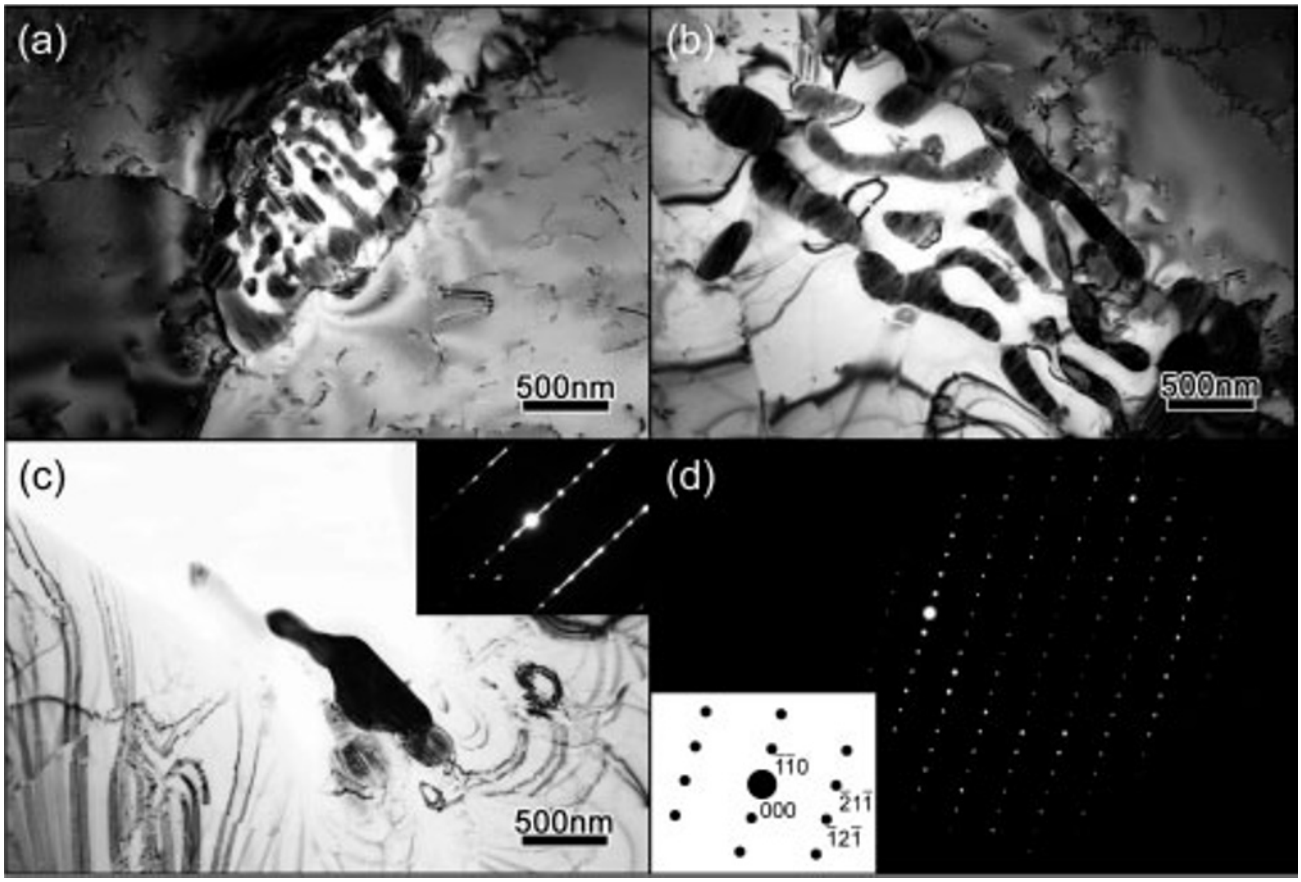

Figure 12 – Higher magnified TEM images of the particles in the regions "A" and "B", and selected area electron diffraction patterns

magnified TEM images of the particles in regions "A" and "B", and the selected area electron diffraction patterns obtained from the particles are shown in Figure 12. The TEM images show that the particles contain numerous stacking faults aligned into a preferential orientation. The electron diffraction pattern reveals that the particle is sigma phase with tetragonal structure, a = 10.9221 Å and c = 5.6403 Å. Closer observation using TEM was also tried to the retreating side of the SZ, but any evidence for the presence of sigma phase was not found in the retreating side.

In the 6 mm-thick weld, ferrite phase was not detected, but they deduced from circumstantial evidence that the sigma phase formation can be accelerated by the emergence of delta-ferrite at high temperatures and the ferrite can further decompose to sigma and austenite phases rapidly under the high strain and recrystallisation [20]. On the other hand, the 2 mm-thick weld does not have any sigma phase in the advancing side of the SZ, but ferrite phase was detected in the SZ although the amount of ferrite was small. This difference in as-welded microstructures between the 2 mm- and 6 mm-thick welds is probably attributed to the difference in the cooling rate due to the differences in plate thickness and travelling speed. The ferrite formed by the exposure to high temperatures during the heating procedure of FSW, even though the formation of ferrite was deduced from the circumstantial evidence in the 6 mm-thick weld, would decompose to sigma and austenite phases during the cooling procedure if the cooling rate was slow. The weld in the thinner plate undergoes the more rapid cooling after the FSW when the FSW parameters are the same. In addition, the travelling speed applied to the 2 mm-thick weld was about 3.4 times faster than that to the 6 mm-thick weld. The increase in the travelling speed increases the cooling rate during FSW. Therefore, the thinner thickness and the higher travelling speed result in an increased cooling rate in the 2 mm-thick weld, which may prevent the decomposition of the ferrite to sigma. This is one of the possible reasons why the ferrite phases remain in some parts of the SZ in the 2 mm-thick weld. The presence of ferrite in the 2 mm-thick weld may confirm that the sigma phase observed in the 6 mm-thick weld can be decomposed from the delta-ferrite formed in the austenite matrix during FSW.

4 CONCLUSION

The microstructure and hardness distribution were examined in friction stir welds of 2 mm- and 6 mm-thick 304 austenitic stainless steel plates. The 2 mm-thick weld had small tunnel-type defects in the advancing side of the SZ. The SZ and TMAZ in the both welds were characterised by dynamically recrystallised and recovered microstructures, respectively. The hardness of the weld was higher than that of the BM. The TMAZ showed the maximum hardness, which was attributed to the slightly finer grain structure having a relatively higher density of sub-boundaries and dislocations. Small ferrite

phases were observed along the grain boundaries of the recrystallised austenite matrix in the advancing side of the SZ in the 2 mm-thick weld, while small sigma phases were detected in the 6 mm-thick weld at roughly the same locations as those of ferrite phases in the 2 mm-thick weld. This suggested that the ferrite was formed during the heating cycle of FSW and then remained due to the higher cooling rate in the thinner weld, while decomposed to sigma due to the lower cooling rate in the thicker weld during FSW.

ACKNOWLEDGEMENTS

The authors are grateful to Mr. A. Honda for technical assistance and thank Prof. K. Ikeda, Prof. K. Maruyama, Prof. Z. J. Wang, Prof. T. W. Nelson and Mr. C. J. Sterling for their helpful discussions. Financial support from the Japanese Ministry of Education, Culture, Sports, Science and Technology for the Promotion of Science with a Grant-in-Aid and for the 21st century COE program in the International Center of Research and Education for Materials at Tohoku University is gratefully acknowledged.

REFERENCES

[1] Dawes C.J., Thomas W.M.: Friction stir process welds aluminum alloys, Weld. J., 1996, vol. 75, No. 3, pp. 41-45.

[2] Thomas W.M., Nicholas E.D.: Friction stir welding for the transportation industries, Mater. Design, 1997, vol. 18, No. 4-6, pp. 269-273.

[3] Liu G., Murr L.E., Niou C.S., McClure J.C., Vega F.R.: Microstructural aspects of the friction-stir welding of 6061-T6 aluminum, Scripta Mater., 1997, vol. 37, No. 3, pp. 355-361.

[4] Sato Y.S., Kokawa H., Enomoto M., Jogan S.: Microstructural Evolution of 6063 Aluminum during Friction-Stir Welding, Metall. Mater. Trans. A, 1999, vol. 30A, No. 9, pp. 2429-2437.

[5] Mahoney M.W., Rhodes C.G., Flintoff J.G., Spurling R.A., Bingel W.H.: Properties of friction-stir-welded 7075 T651 aluminum, Metall. Mater. Trans. A, 1998, vol. 29A, No. 7, pp. 1955-1964.

[6] Sato Y.S., Kokawa H.: Distribution of tensile property and microstructure in friction stir weld of 6063 aluminum, Metall. Mater. Trans. A, 2001, vol. 32A, No. 12, pp. 3023-3031.

[7] Lumsden J.B., Mahoney M.W., Rhodes C.G., Pollock G.A.: Corrosion behavior of friction-stir-welded AA7050-T7651, Corrosion, 2003, vol. 59, No. 3, pp. 212-219.

[8] Colligan K.: Material flow behavior during friction stir welding of aluminum, Weld. J., 1999, vol. 78, No. 7, pp. 229S-237S.

[9] Reynolds A.P.: Visualisation of material flow in autogenous friction stir welds, Sci. Technol Weld. Join., 2000, vol. 5, No. 2, pp. 120-124.

[10] Li Y., Murr L.E., McClure J.C.: Solid-state flow visualization in the friction-stir welding of 2024 Al to 6061 Al, Scripta Mater., 1999, vol. 40, No. 9, pp. 1041-1046.

[11] Li Y., Trillo E.A., Murr L.E.: Friction-stir welding of aluminum alloy 2024 to silver, J. Mater. Sci. Let., 2000, vol. 19, No. 12, pp. 1047-1051.

[12] Sato Y.S., Park S.H.C., Michiuchi M., Kokawa H.: Constitutional liquation during dissimilar friction stir welding of Al and Mg alloys, Scripta Mater., 2004, vol. 50, No. 9, pp. 1233-1236.

[13] Sato Y.S., Urata M., Kokawa H., Ikeda K., Enomoto M.: Retention of fine grained microstructure of equal channel angular pressed aluminum alloy 1050 by friction stir welding, Scripta Mater., 2001, vol. 45, No. 1, pp. 109-114.

[14] Sato Y.S., Urata M., Kokawa H., Ikeda K.: Hall-Petch relationship in friction stir welds of equal channel angular pressed aluminium alloys, Mater. Sci. Eng. A, 2003, vol. A354, No. 1-2, pp. 298-305.

[15] Sato Y.S., Kurihara Y., Park S.H.C., Kokawa H., Tsuji N.: Friction stir welding of ultrafine grained Al alloy 1100 produced by accumulative roll-bonding, Scripta Mater., 2004, vol. 50, No. 1, pp. 57-60.

[16] Thomas W.M., Threadgill P.L., Nicholas E.D.: Feasibility of friction stir welding steel, Sci. Technol. Weld. Join., 1999, vol. 4, No. 6, pp. 365-372.

[17] Lienert T.J., Stellwag W.L., Grimmett B.B., Warke R.W.: Friction stir welding studies on mild steel, Weld. J., 2003, vol. 82, No. 1, pp. 1S-9S.

[18] Reynolds A.P., Tang W., Gnaupel-Herold T., Prask H.: Structure, properties, and residual stress of 304L stainless steel friction stir welds, Scripta Mater., 2003, vol. 48, No. 9, pp. 1289-1294.

[19] Park S.H.C., Sato Y.S., Kokawa H., Okamoto K., Hirano S., Inagaki M.: Rapid formation of the sigma phase in 304 stainless steel during friction stir welding, Scripta Mater., 2003, vol. 49, No. 12, pp. 1175-1180.

[20] Park S.H.C., Sato Y.S., Kokawa H., Okamoto K., Hirano S., Inagaki M.: Corrosion resistance of friction stir welded 304 stainless steel, Scripta Mater., 2004, vol. 51, No. 2, pp. 101-105.

[21] Okamoto K., Hirano S., Inagaki M., Park S.H.C., Sato Y.S., Kokawa H., Nelson T.W., Sorensen C.D.: Metallurgical and mechanical properties of friction stir welded stainless steels, 2003, Proc. 4th Int. Sympo. on Friction Stir Welding, Park City, Utah, TWI, CD-ROM.

[22] Park S.H.C., Sato Y.S., Kokawa H., Okamoto K., Hirano S., Inagaki M.: Microstructural characterisation of the stir zone containing residual ferrite in friction stir welded 304 austenitic stainless steel, Sci. Technol. Weld. Join., 2004, submitted.

[23] Sorensen C.D., Nelson T.W.: Progress in polycrystalline cubic boron nitride FSW tooling, 2003, Proc. 4th Int. Sympo. on Friction Stir Welding, Park City, Utah, TWI, CD-ROM.

[24] Di Schino A., Kenny J.M.: Grain refinement strengthening of a micro-crystalline high nitrogen austenitic stainless steel, Mater. Lett., 2003, vol. 57, No. 12, pp. 1830-1834.

[25] Park S.H.C., Sato Y.S., Kokawa H.: Basal plane texture and flow pattern in friction stir weld of a magnesium alloy, Metall. Mater. Trans. A, 2003, vol. 34A, No. 4, pp. 987-994.